Supporting information

Human exposure to air contaminants under the far-UVC system operation in an office: Effects of lamp position and ventilation condition

Seongjun Park[1], *Donghyun Rim*[1*]

[1] Department of Architectural Engineering, Pennsylvania State University, University park, PA, 16802, USA

[*]Corresponding author: Donghyun Rim

Pennsylvania State University, University park, PA, 16802, USA

dxr51@psu.edu

The content of the supporting information is:

S1. CFD model setup and boundary conditions.

For mixing ventilation, two four-way ceiling diffusers supplied the air jet angled at 30° toward the ceiling. The total air inlet and exhaust areas were 0.15 and 0.45 m^2, respectively (Figure S1). The infiltration (or natural ventilation) was simulated as displacement ventilation because they have both a buoyancy-driven airflow pattern [1,2]. Under infiltration, the low-momentum air was supplied through the area inlet with an area of 0.52 m^2 (Figure S1). The supply air was 100% outdoor air, and its temperature was set to satisfy the room air temperature of 298 K. The metabolic heat of each occupant, 99 W (seating mode), was divided into the convective load (40%) and the radiative load (60%) [3]. The convective load was applied to the human surface, while the radiative load was modeled as a heat flux to walls, floor, and ceiling [4]. Note that there is no heat exchange through walls, floor, and ceiling.

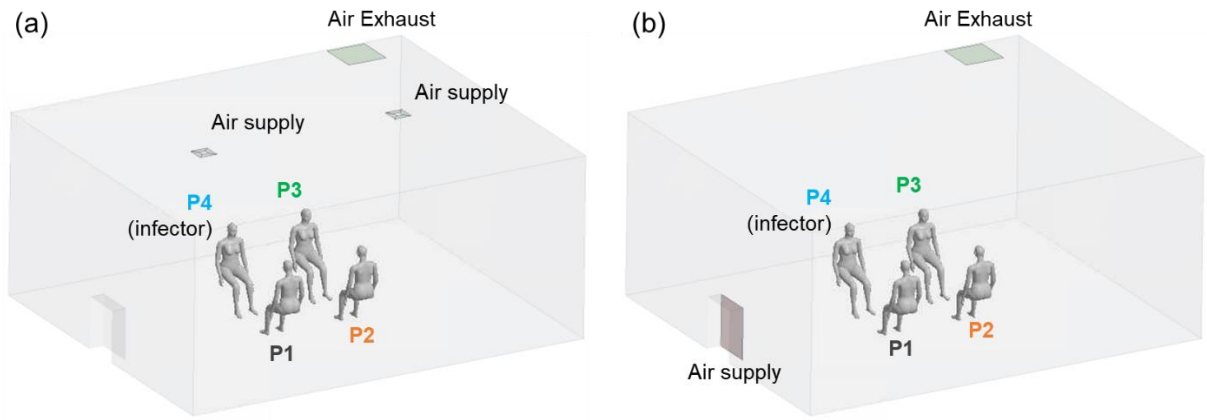

Figure S1. Model geometry: (a) mixing ventilation and (b) infiltration (displacement ventilation).

We used a commercial CFD solver, STAR-CCM+ version 2021.03. The airflow field was calculated using Large Eddy Simulation (LES). This turbulence model can simulate the large-scale turbulent eddies so that it has a good accuracy in calculating the mass and heat transport [5,6]. Airborne pathogens were modeled as a liquid-phase particle with a size of 1 μm and a density of 1000 $kg \cdot m^{-3}$ using the Eulerian approach [7,8]. The particle deposition is an important particle loss mechanism, so we applied the deposition velocity on the floor with a deposition velocity of 0.003 $cm \cdot s^{-1}$ [9]. Note that the particle size change due to the coagulation and evaporation was not considered in this study. We chose the polyhedral mesh to create the mesh in the simulation domain due to its good accuracy in predicting the gradients near wall regions [10] (Figure S2). Based on the previous study's mesh sensitivity analysis, we set the mesh sizes as follows [11]: The base cell size – 0.15 m, the first cell size (near human surface) – 0.01 m, the human surface cell size – 0.01 m, inlet and outlet cell sizes – 0.01 m. Note that the average y+ value of human surface was 3.5 and the total cell number within the simulation domain was 470K.

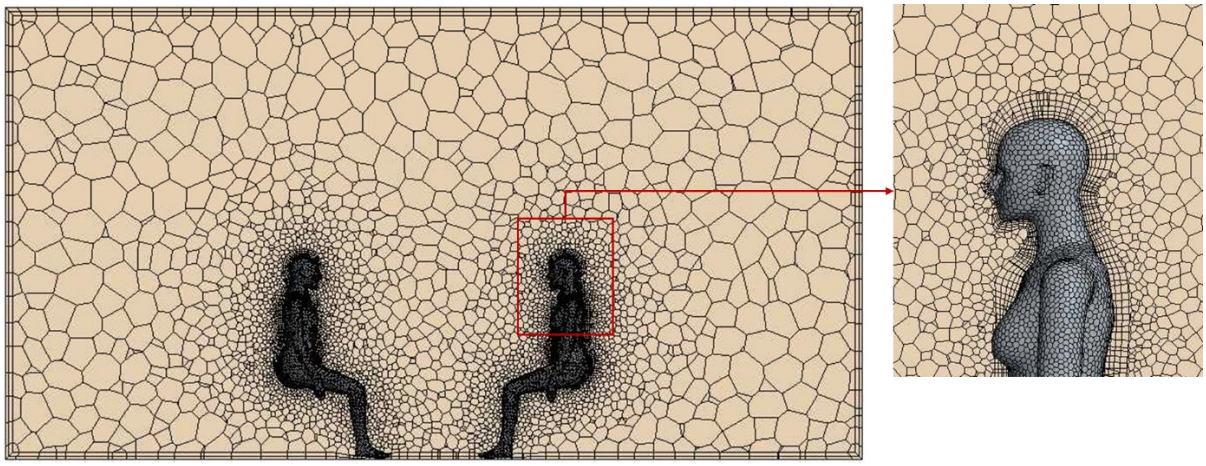

Figure S2. Mesh view.

S2. Chemistry modeling.

In the CFD simulation, we employed the unsteady-state multi-component gas model to simulate a total of 12 chemical reactions (Table S1). These chemical reactions were based on Barber et al. (2023) [12]. Note that the VOCs have the same rate constant as limonene. The rate constants of chemical reactions 1 -3 were determined by the UV fluence rate. As we modeled the spatial distributions of UV fluence rate produced by different far-UVC lamp types, we incorporated the corresponding rate constants for each lamp type into the CFD simulation. Thus, as getting close to the far-UVC lamp, the UV fluence rate and the rate constant of chemical reactions 1-3 increase. The human skin oil reaction with O_3 and VOCs was not considered in this study.

In the CFD model, the airflow field was calculated using LES (S1. CFD model setup and boundary conditions), and the transport and reaction of gas-phase compounds was calculated as follows [11]:

$$\frac{\partial}{\partial t}(\rho C_i) + \frac{\partial}{\partial x}(\rho u C_i) = \frac{\partial}{\partial x}\left(\rho D \frac{\partial C_i}{\partial x}\right) + S_i + R_i \quad \text{(Eq. S1)}$$

where ρ is the density of air, C_i is the mole fraction of chemical species, u is the velocity of air, D is the molecular diffusion coefficient; S_i is the source term or sink term (i.e., emission of chemical species or ozone deposition), and R_i is the chemical reaction term. In the simulation, R_i is defined as follows [13]:

$$R_i = M_i \sum_{r=1}^{N} R_{i,r} \quad \text{(Eq. S2)}$$

Where, M_i is the molecular weight of ith species, N_r is the number of chemical reactions, and $R_{i,r}$ is the molar rate of generation or loss of ith species in the reaction r. The reaction term was the net production and consumption rate due to chemical reactions for each chemical component.

Table S1. Chemical reactions modeled in this study. Note that I^* is the UV fluence rate.

No	Reactants		Products		Rate constant	Unit
1	O_2		2O		4.78×10^{-12}	$\times I^* s^{-1}$
2	O_3		$O(^1D)$	O_2	1.48×10^{-11}	$\times I^* s^{-1}$
3	O_3		O	O_2	5.07×10^{-12}	$\times I^* s^{-1}$
4	O	O_2	O_3		1.5×10^{-14}	$cm^3 \cdot mol^{-1} \cdot s^{-1}$
5	H_2O	(O^1D)	2OH		2×10^{-10}	$cm^3 \cdot mol^{-1} \cdot s^{-1}$
6	O	O_3	$2O_2$		8×10^{-15}	$cm^3 \cdot mol^{-1} \cdot s^{-1}$
7	OH	O_3	HO_2	O_2	7.25×10^{-14}	$cm^3 \cdot mol^{-1} \cdot s^{-1}$
8	OH	HO_2	H_2O	O_2	1.11×10^{-10}	$cm^3 \cdot mol^{-1} \cdot s^{-1}$
9	HO_2	O_3	OH	$2O_2$	2.01×10^{-15}	$cm^3 \cdot mol^{-1} \cdot s^{-1}$
10	$O(^1D)$		O		8×10^{8}	s^{-1}
11	VOCs	O_3	Product	0.86OH	2×10^{-16}	$cm^3 \cdot mol^{-1} \cdot s^{-1}$
12	VOCs	OH	Product		1.71×10^{-10}	$cm^3 \cdot mol^{-1} \cdot s^{-1}$

S3. CFD model validation.

We validated our CFD model with four steps: 1) Airflow field and particle transport, 2) time-series airborne pathogen concentration, 3) O_3 generation by indoor chemical reactions, and 4) O_3 deposition on surrounding and human surfaces.

1) The validation of the airflow field and particle transport

To validate the airflow field, we compared the simulated vertical air velocity with the experiment. The CFD model geometry and all boundary conditions were generated based on the experiment conducted by Liu et al. (2022) [14]. The ventilation rate was 4 h^{-1} for both mixing and displacement ventilations, with a total thermal load of 113 $W \cdot m^{-2}$. The air jet velocity and particle flow rate from an infector were adjusted to 1.6 $m \cdot s^{-1}$ and 3×10^{-3} $ml \cdot min^{-1}$, respectively, with a particle size of 0.4 μm.

Figure S3 shows the vertical air velocity from the CFD model and measurement at the steady state. Note that P5 – 8 represent the sampling points. The mean differences between the CFD model and measurement of mixing and displacement ventilations are 0.03 $m \cdot s^{-1}$ (20%) and 0.04 $m \cdot s^{-1}$ (37%). The CFD model and experiment results do not perfectly match, however, the figure shows that the CFD model with a turbulent model, LES, can create a vertical air velocity profile similar to the experiment.

Figure S4 shows the vertical particle concentration from the CFD model and measurement at the steady state. Note that the concentration is normalized by the exhaust concentration.

$$C^* = \frac{C - C_s}{C_e - C_s} \quad \text{(Eq. S3)}$$

Where, C is the particle concentration at each point, and C_e, and C_s are the particle concentration at the exhaust and supply, respectively.

According to the figure, the particle concentrations predicted by the CFD model agree well with the experiment with a mean difference less than 0.24 (20%). Similar to the airflow field, the CFD model does not achieve perfect particle concentration prediction compared to the experiment. Nevertheless, our CFD model demonstrates a reasonable capability in predicting both the airflow field and particle concentration in comparison to the experimental results.

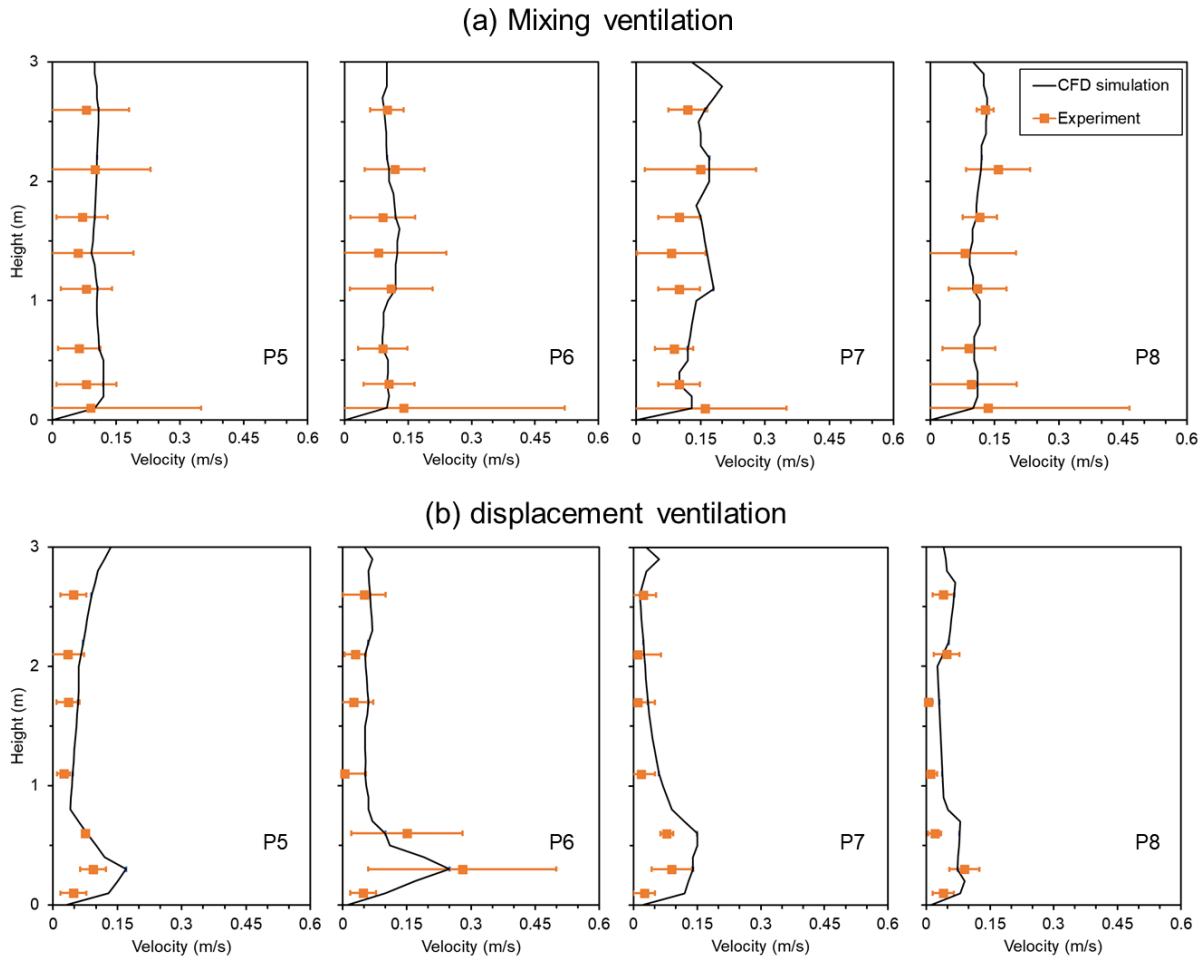

Figure S3. Vertical air velocity profile from the CFD model and measurement: (a) mixing ventilation and (b) displacement ventilation. Note that P5 – 8 are the sampling points.

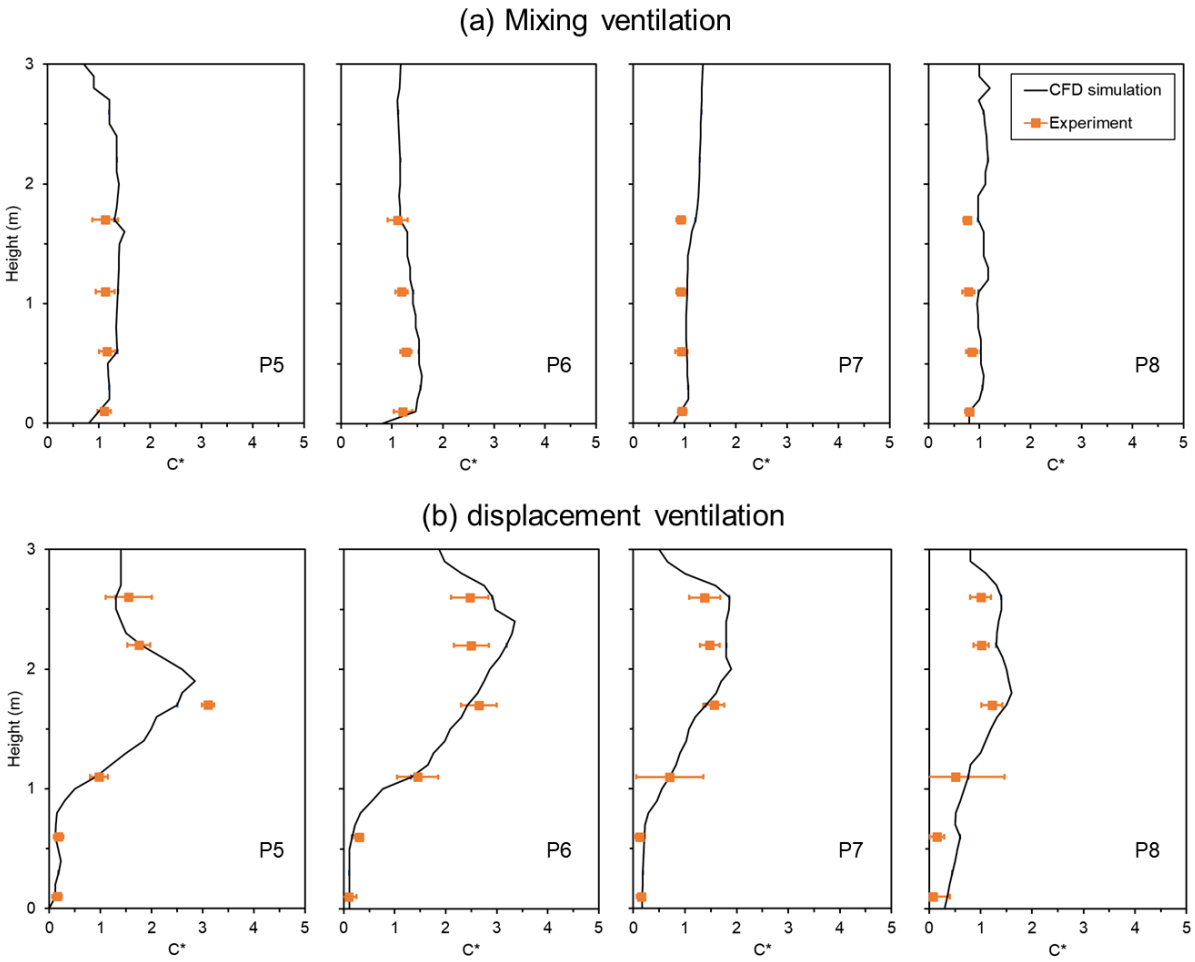

Figure S4. Vertical particle concentration profile from the CFD model and measurement: (a) mixing ventilation and (b) displacement ventilation. Note that P5 – 8 are the sampling points, and the concentration is normalized by the exhaust concentration (Eq. S3).

2) Time-series airborne pathogen concentration.

To make sure that our CFD model can predict the time-series airborne pathogen concentration, we compared the breathing zone concentrations from the CFD model and the mass balance model (Eq. S4) [15]. The airborne pathogens were emitted from an infector's mouth (1.2 cm^2) with an air speed of 4 $m \cdot s^{-1}$ and a concentration of 1 $\mu g \cdot m^3$. The ventilation condition was the

mixing ventilation with a ventilation rate of 0.7 h^{-1}, and the particle deposition was modeled on the floor with a deposition velocity of 0.003 $cm \cdot s^{-1}$.

$$\frac{dC_{in}(t)}{dt} = aC_{out}(t) - (k + \mathrm{a})C_{in}(t) + \frac{E(t)}{V} \quad \text{(Eq. 3)}$$

Where $C_{in}(t)$ is the indoor O_3 concentration at time, t (ppb), $C_{out}(t)$ is the outdoor O_3 concentration at time, t (ppb), a is the air change rate (h^{-1}), k is the deposition rate (h^{-1}), $E(t)$ is the emission rate at time t $(\mu g \cdot h^{-1})$, and V is the total room volume (m^3).

Figure S5 illustrates the comparison between the room average time-series airborne pathogen concentrations calculated by the CFD model and the mass balance model. The concentration differences between two models were less than 5%, which confirms that our CFD model can predict the time-series airborne pathogen concentration.

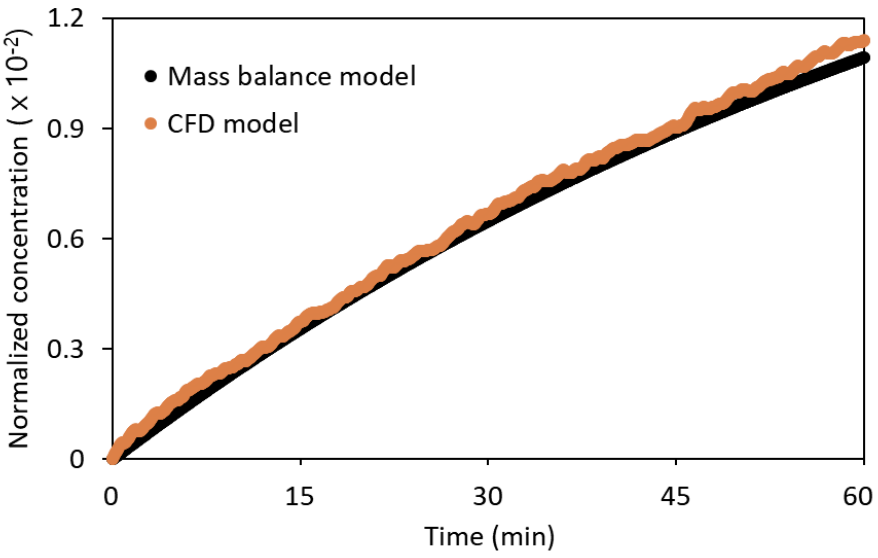

Figure S5. Time-series breathing zone airborne pathogen concentration calculated by the CFD model and the mass balance model.

3) O_3 generation by indoor chemical reactions.

We also compared the time-series O_3 concentration from our CFD model and the chamber experiment conducted by Barber et al. (2023) [12]. The CFD simulation domain, boundary conditions, and chemical reactions applied to the CFD model were based on the experimental setup and Table S1 [12]. The time-series O_3 concentrations calculated by the CFD model (multi-component gas model with LES) show a good agreement with the experiment (Figure S6). This result demonstrates the capability of our CFD model to predict the O_3 generation associated with indoor chemical reactions as outlined in Table S1.

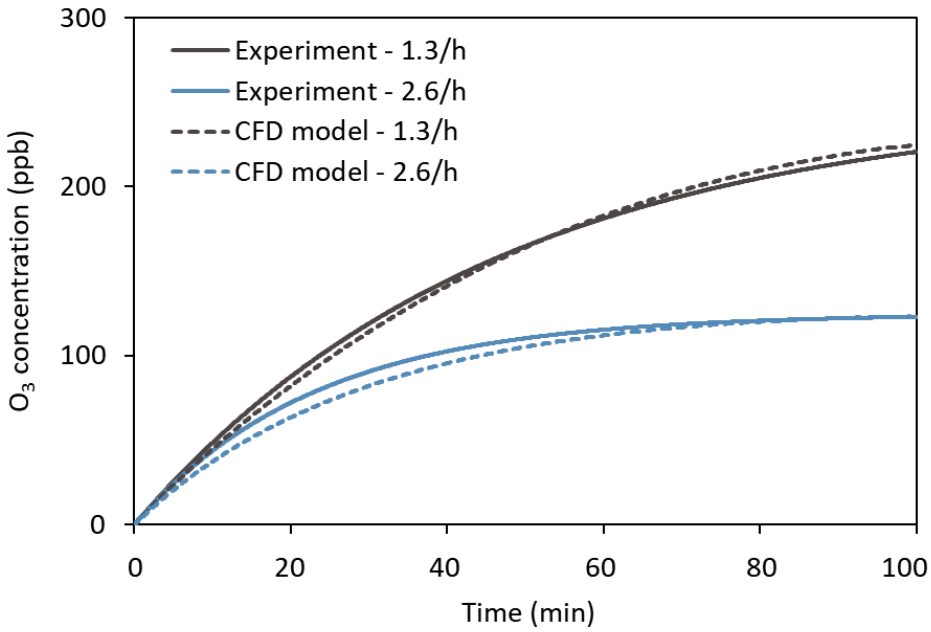

Figure S6. Time-series O_3 concentration from the CFD model and the experiment.

4) O_3 deposition on surrounding and human surfaces.

Lasty, we compared the O_3 concentrations calculated by the CFD model and the mass balance model (Eq. S3) to validate to validate the CFD model's ability to predict indoor O_3 concentration, considering O_3 deposition on indoor surfaces (surrounding walls and human). The simulation domain and boundary conditions are described in Section S1. As the mass balance model assumes a perfect mixing condition, this validation was carried out under mixing ventilation. The chemical reactions in Table S1 were not modeled for this test. There was no O_3 source indoors and O_3 was introduced only from outdoors with a concentration of 40 ppb. The O_3 deposition rate on surrounding surfaces (walls, floor, and ceiling) was 2.8 [16], and the O_3 deposition velocity on the human surface was 6.8 $m \cdot h^{-1}$ [13]. Table S2 shows the room average O_3 concentration calculated by the CFD model and the mass balance model at the steady state. The result indicates a good agreement between the O_3 concentration predicted by our CFD model and the mass balance model, with differences of less than 15%.

Table S2. Room average O_3 concentration calculated by the CFD model and the mass balance model.

Ventilation rate (h^{-1})	O_3 concentration (ppb)	
	CFD model	Mass balance model
0.7	9.6 (± 0.4)	8.4
2	19.0 (± 0.3)	17.0
4	24.0 (± 0.3)	23.8

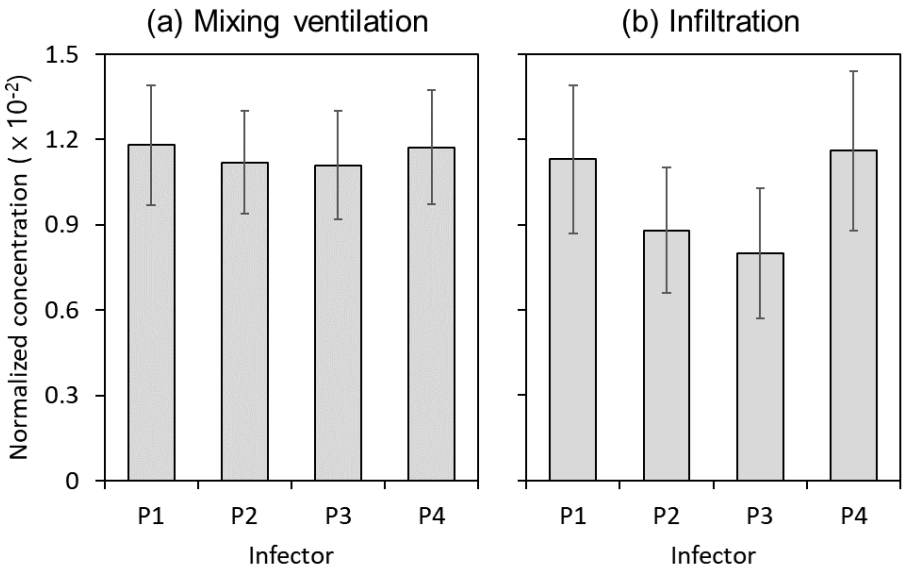

Figure S7. Airborne pathogen concentration within the breathing zone at one hour: (a) mixing ventilation and (b) infiltration (displacement ventilation). Note that the ventilation rate is 0.7 h^{-1}, and the concentration is normalized by the emission concentration.

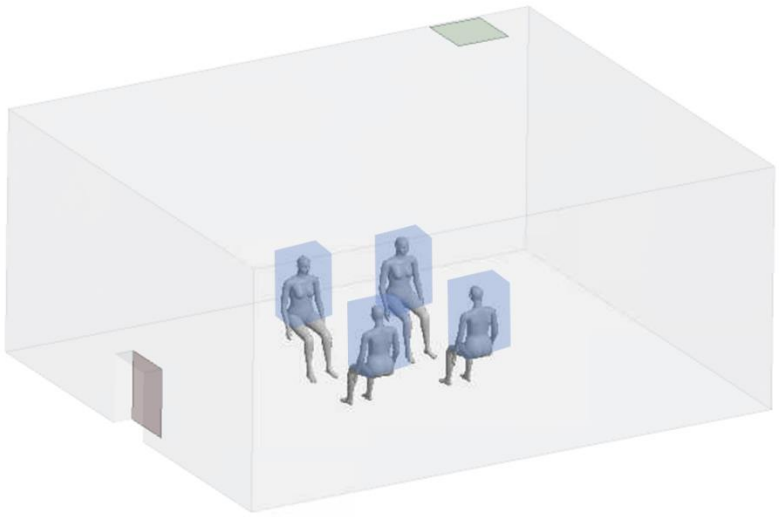

Figure S8. Human envelope zone (Blue box - defined as a 0.8 m^3 box air volume near the human body) [13].

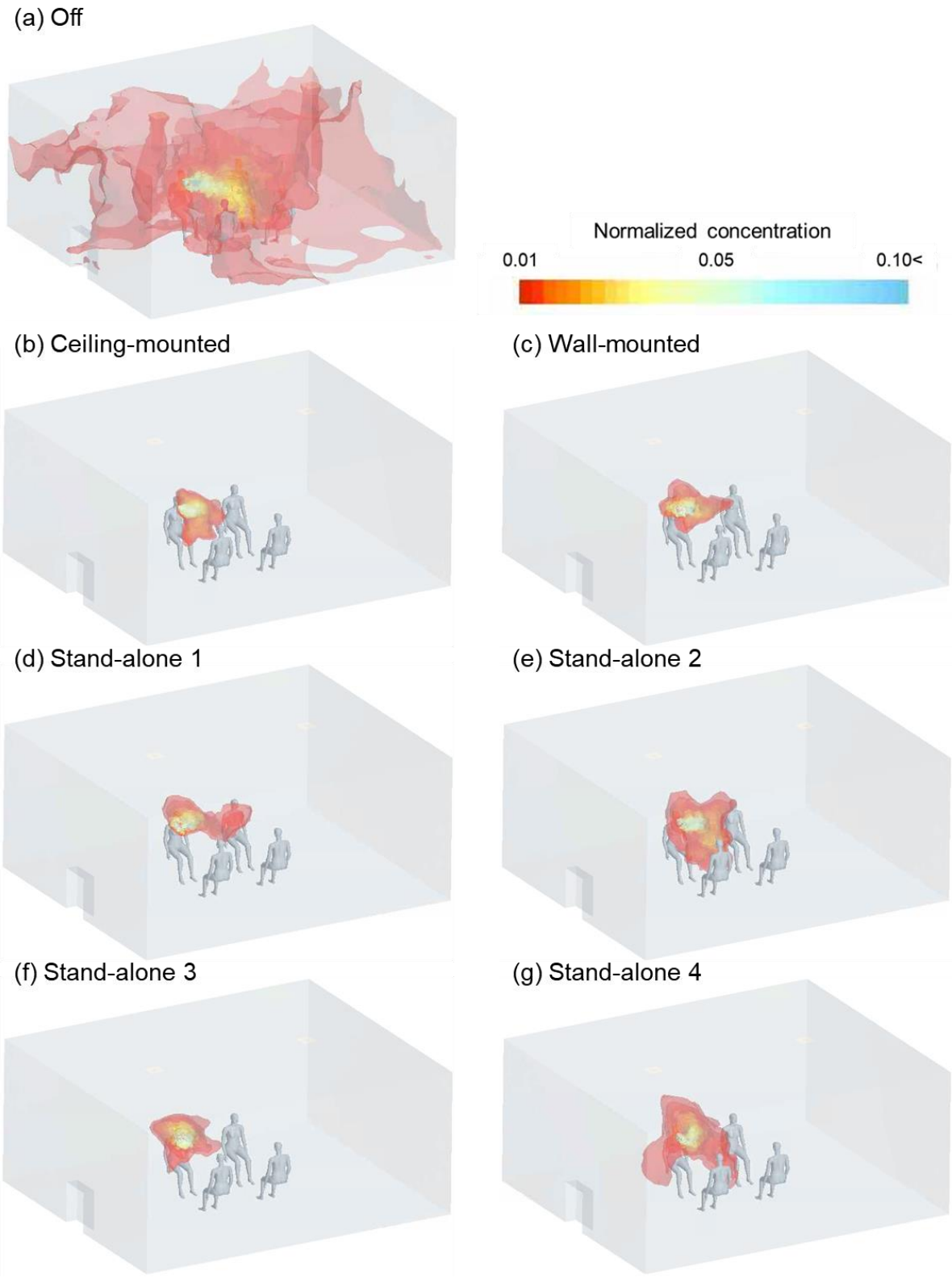

Figure S9. Airborne pathogen concentration contour at one hour under mixing ventilation (0.7 h^{-1}). Note that the concentration is normalized by the emission concentration.

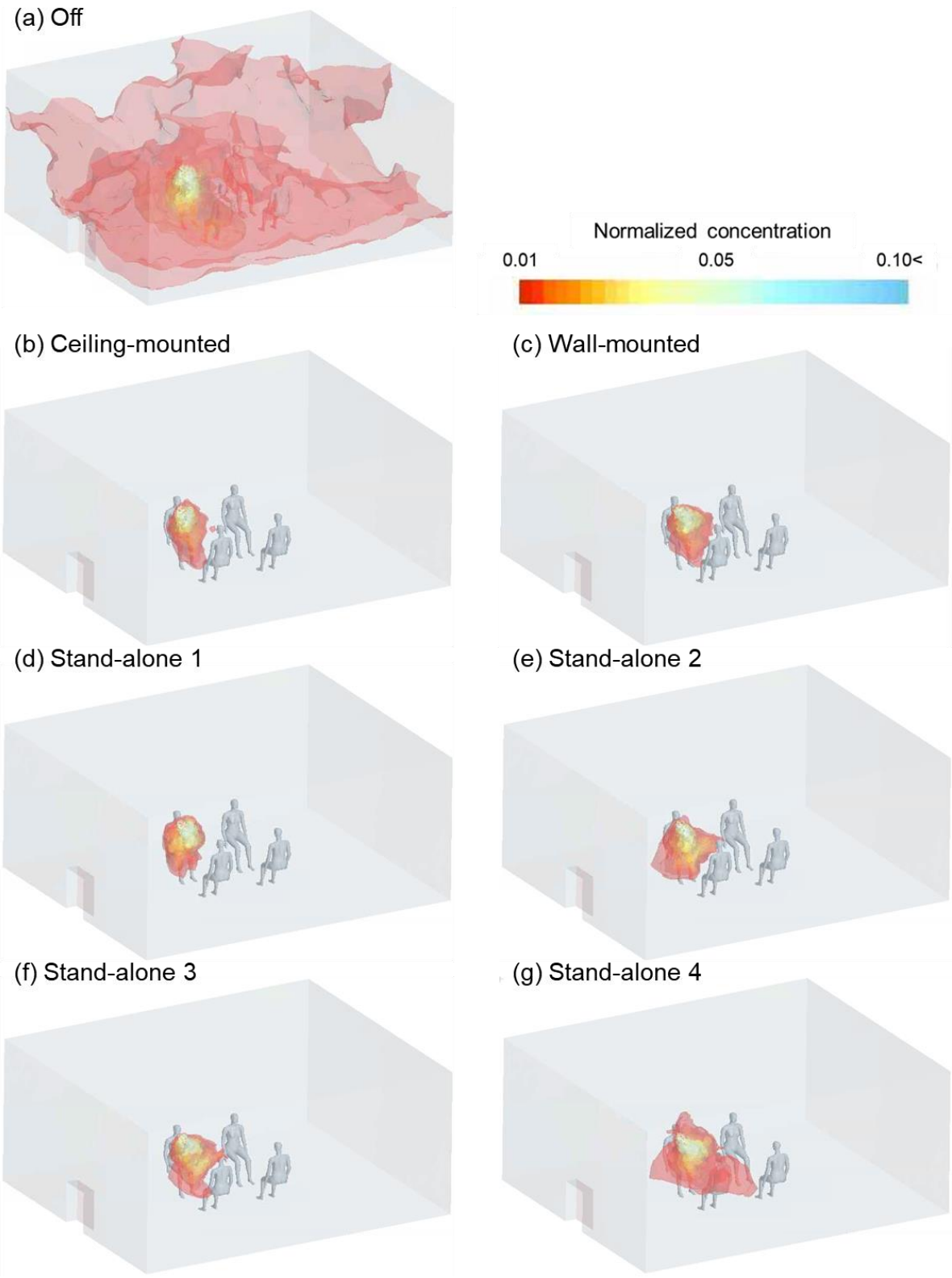

Figure S10. Airborne pathogen concentration contour at one hour under infiltration (0.7 h^{-1}). Note that the concentration is normalized by the emission concentration.

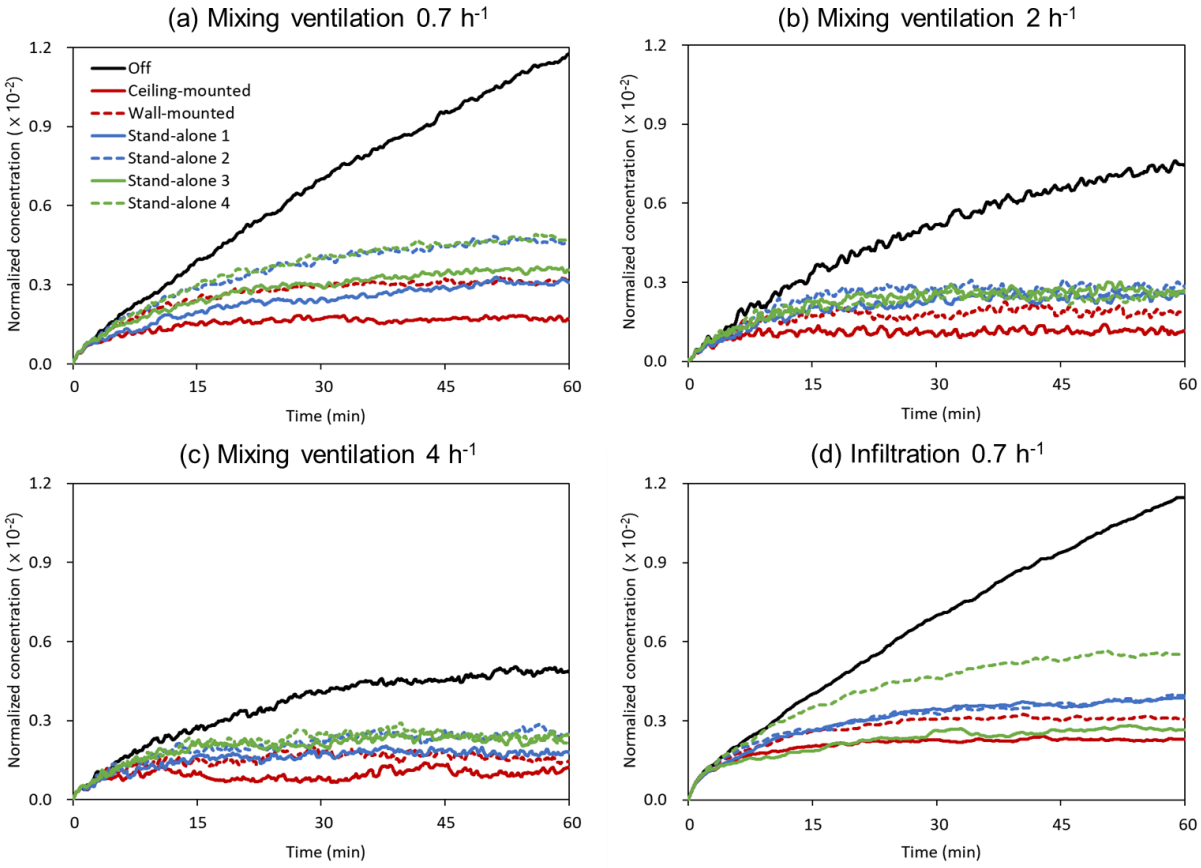

Figure S11. Time-series airborne pathogen concentration within the ASHRAE breathing zone. Note that the concentration is normalized by the emission concentration.

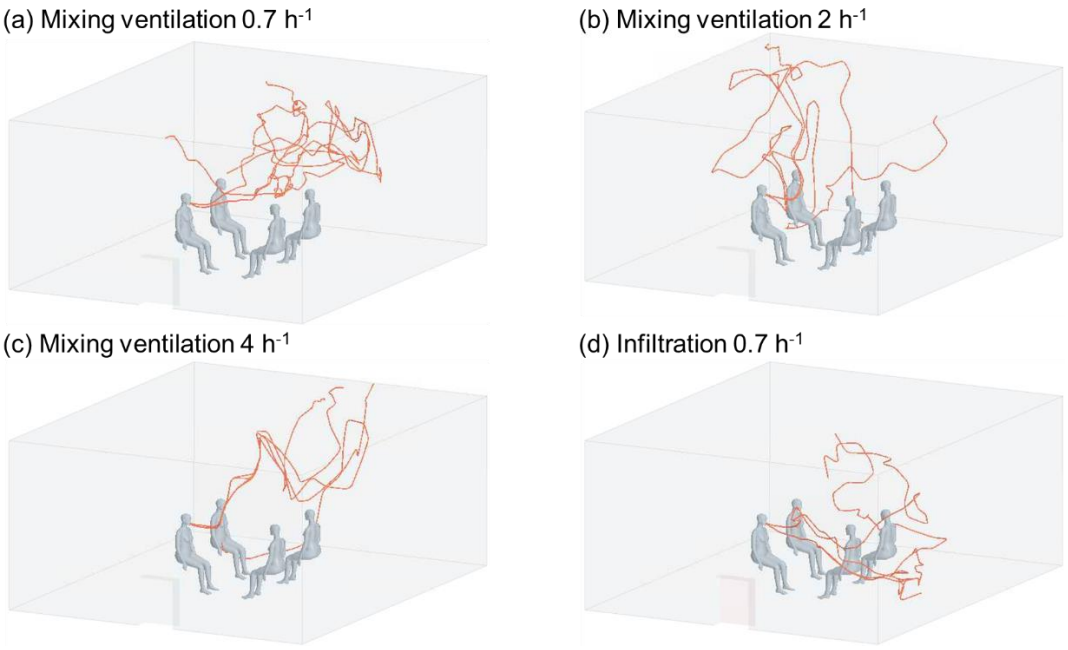

Figure S12. Trajectory of airborne pathogens from an infector.

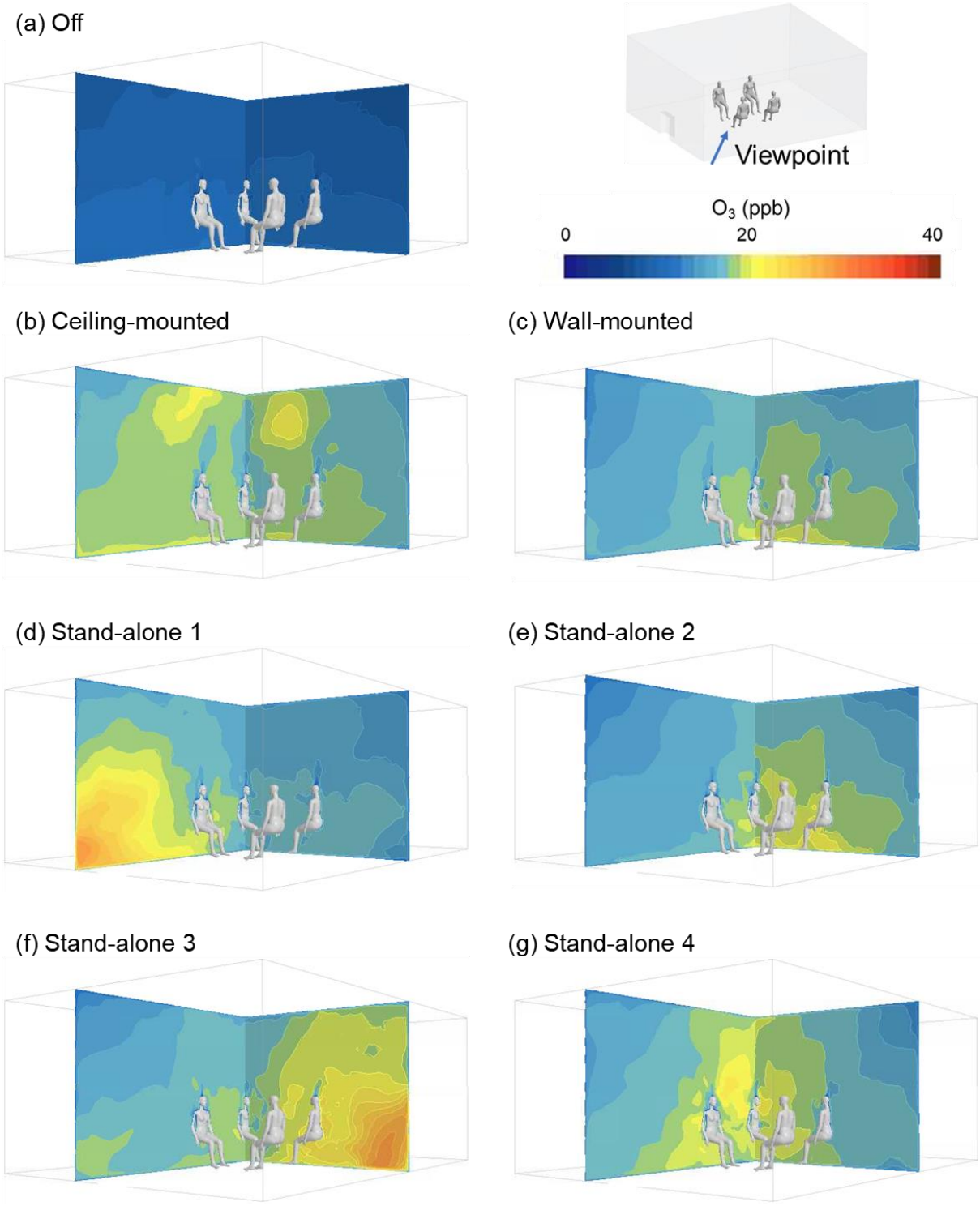

Figure S13. O_3 concentration contour at one hour under mixing ventilation (0.7 h^{-1}) – viewpoint 1.

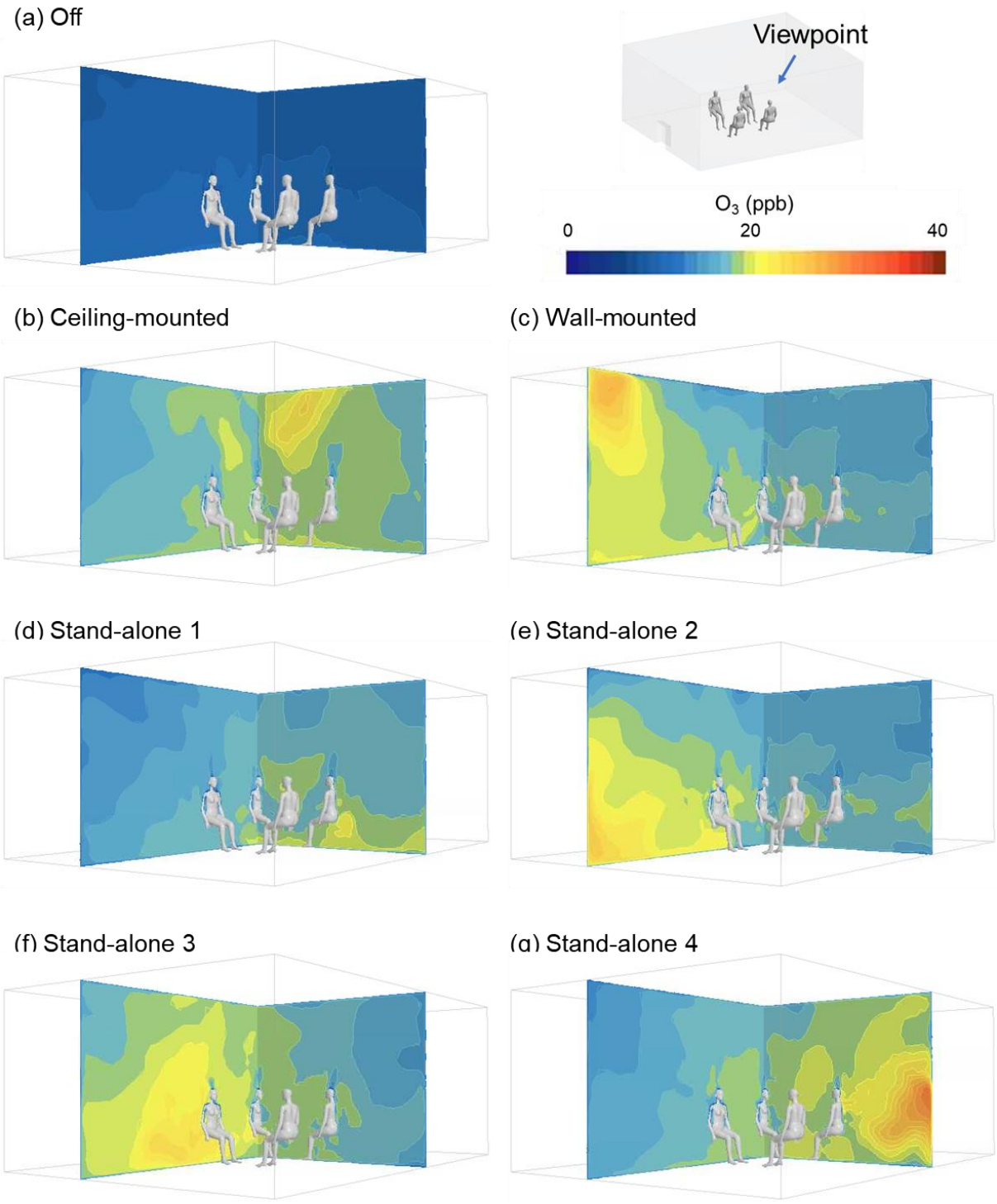

Figure S14. O_3 concentration contour at one hour under mixing ventilation (0.7 h^{-1}) – viewpoint 2.

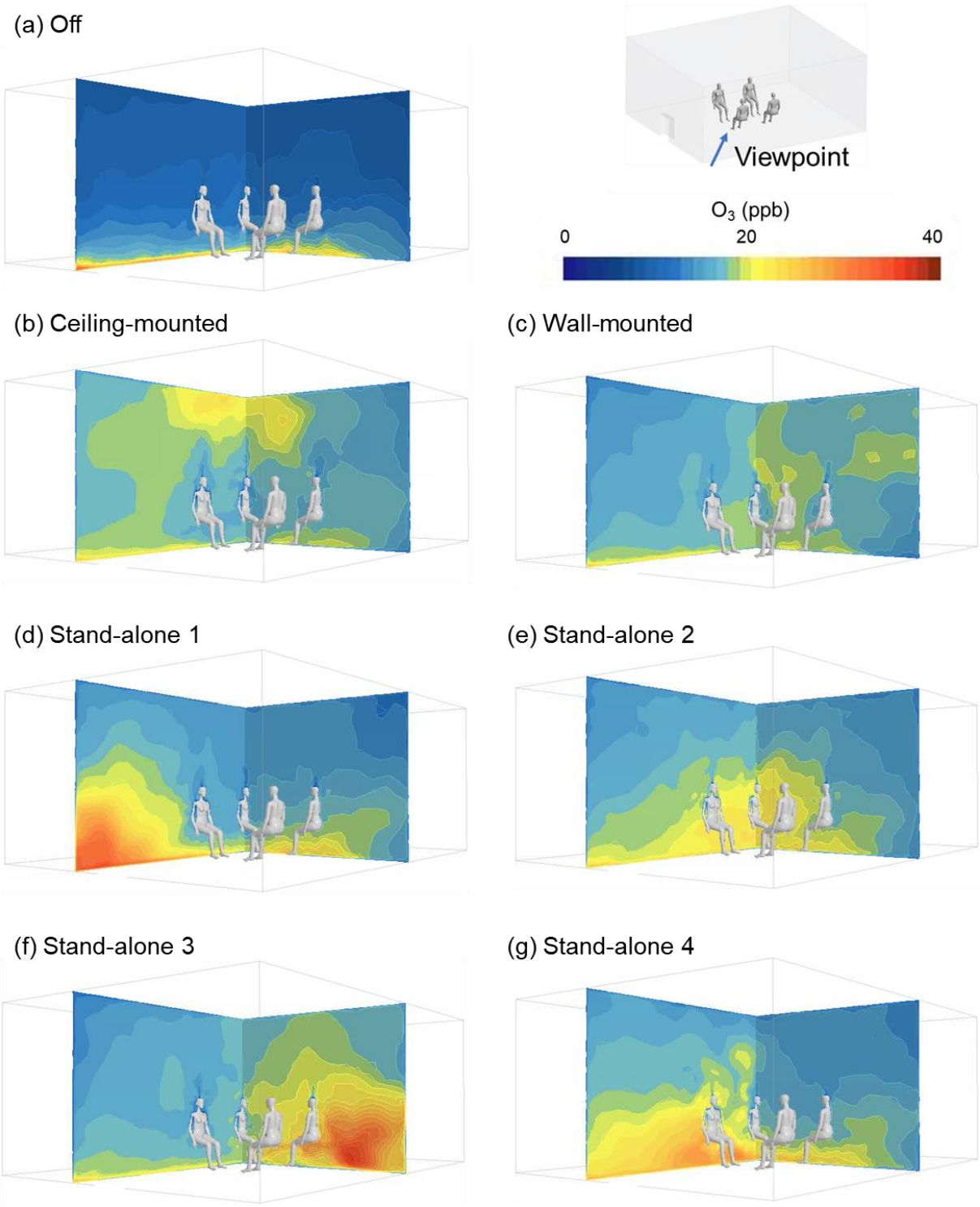

Figure S15. O_3 concentration contour at one hour under infiltration (0.7 h^{-1}) – viewpoint 1.

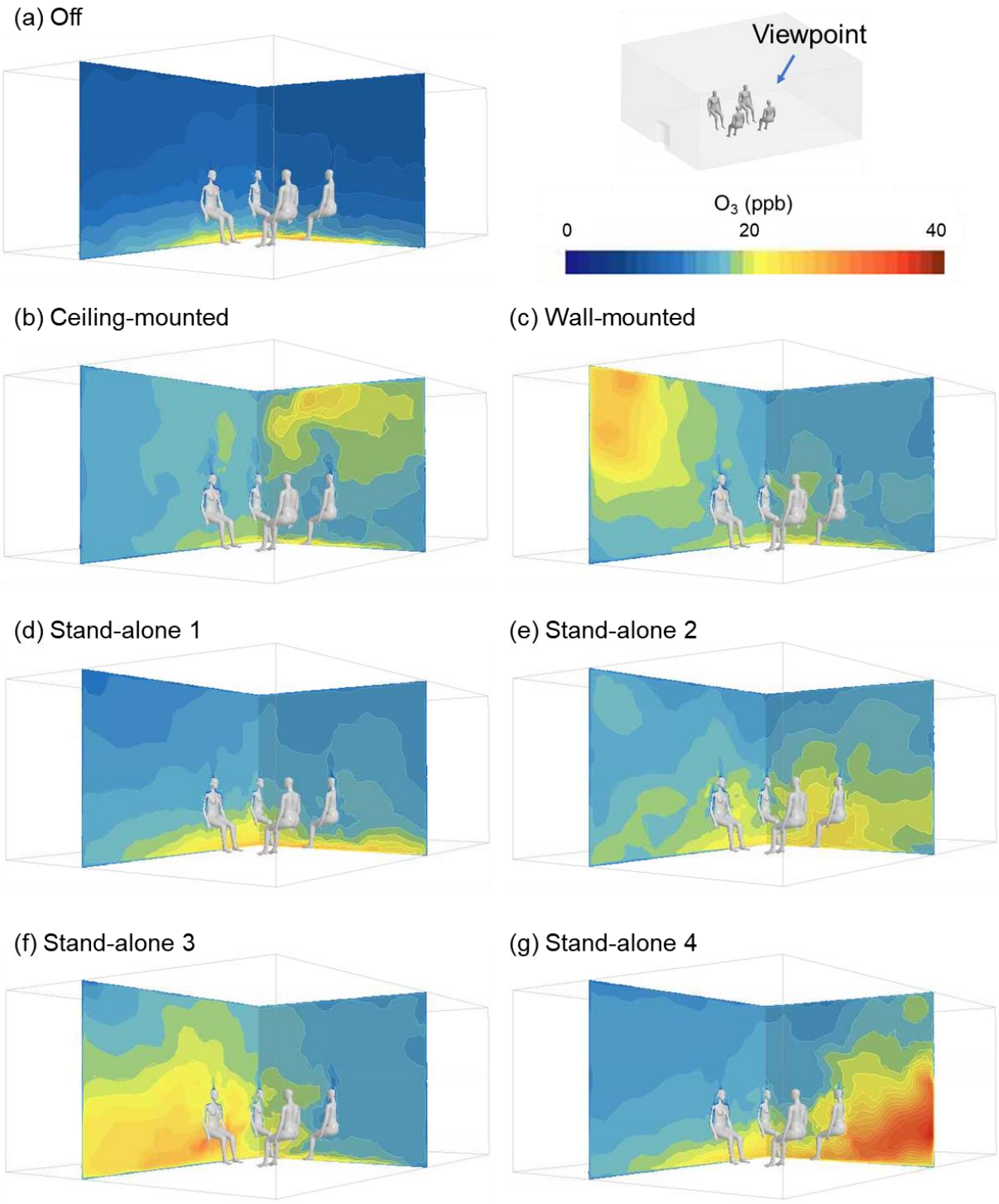

Figure S16. O_3 concentration contour at one hour under infiltration (0.7 h^{-1}) – viewpoint 2.

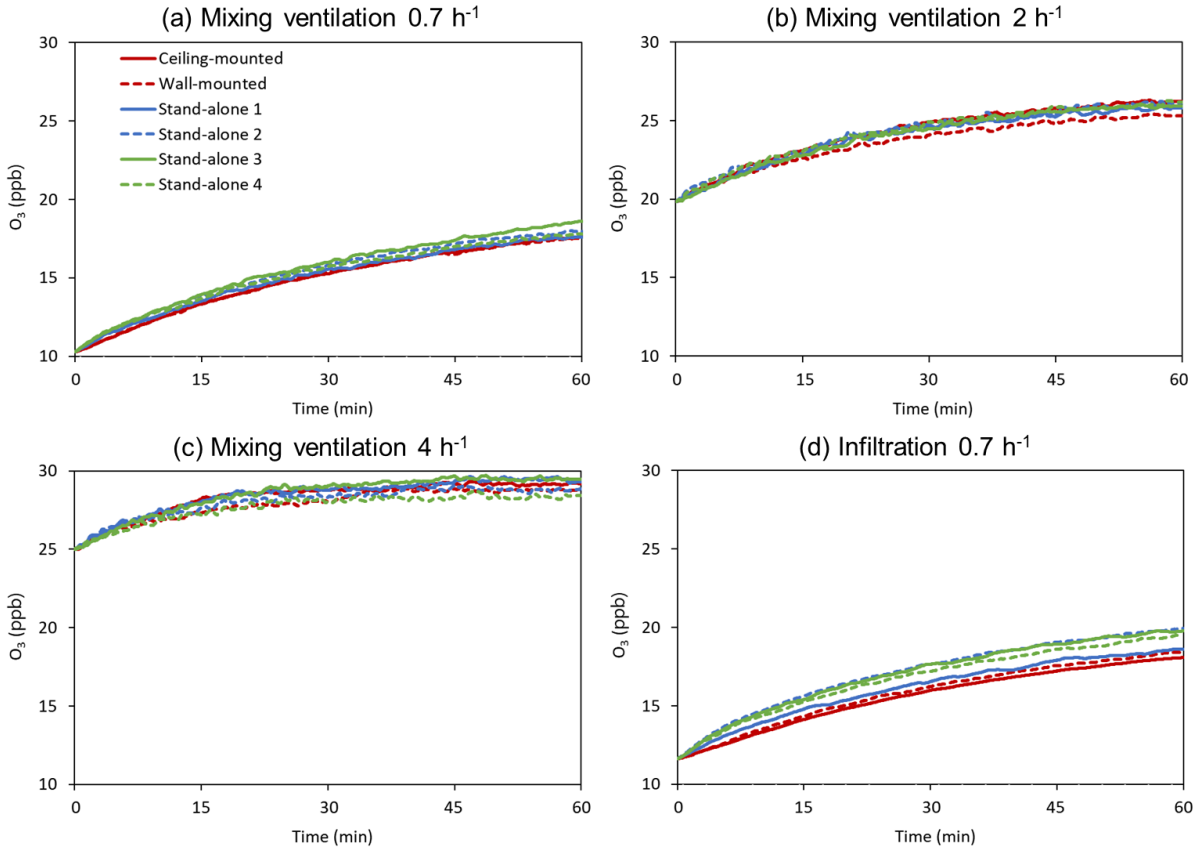

Figure S17. Time-series O_3 concentration within the ASHRAE breathing zone. Note that the far-UVC system activated after occupants had been in the room for one hour. Thus, the concentration at a time step of 0 represents the concentration at one hour without the far-UVC operation.

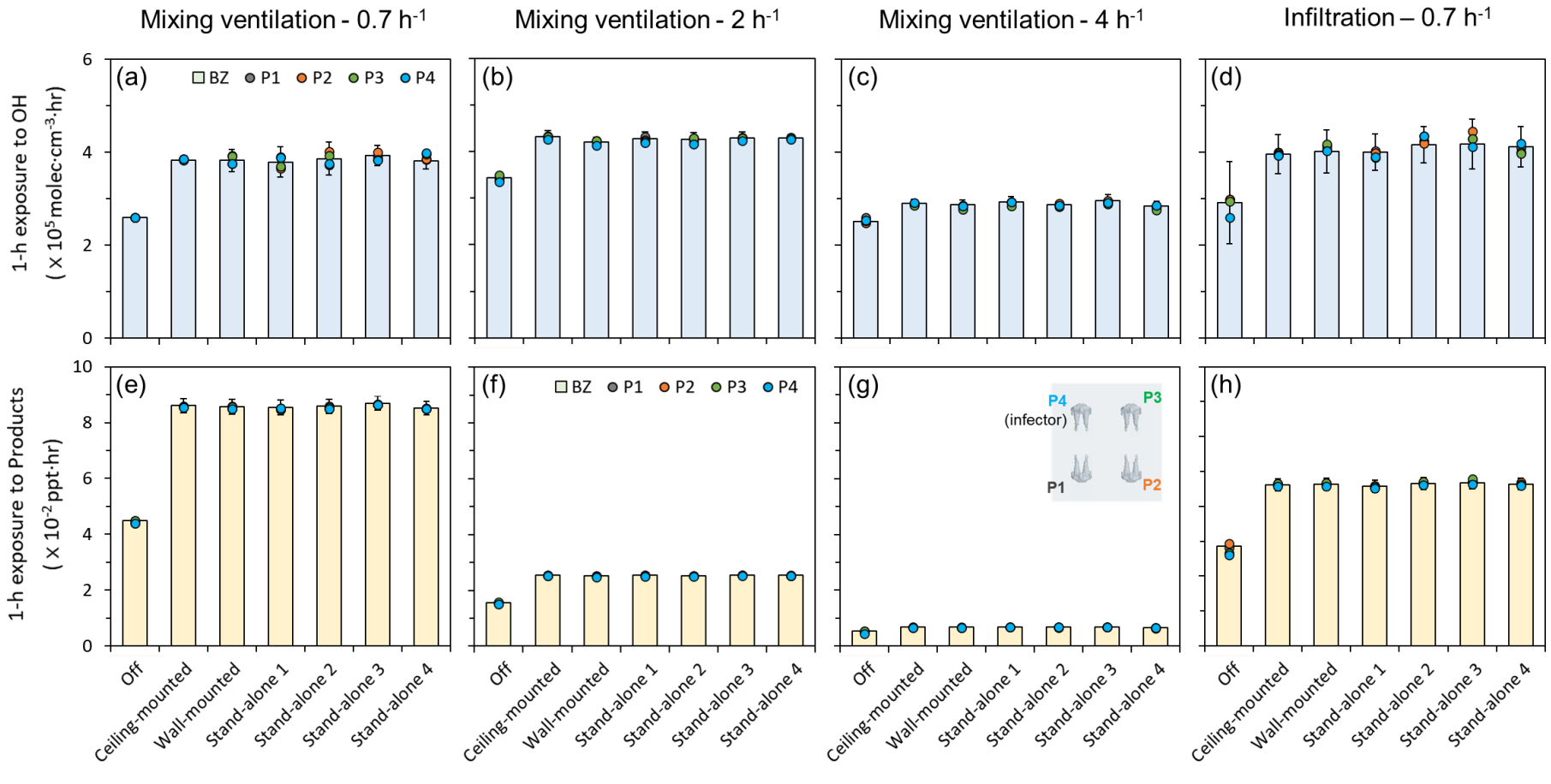

Figure S18. 1-hr exposure to OH (a, b, c, and d) and products (e, f, g, and h). Note that BZ is the ASHRAE breathing zone average concentration (defined as the air volume ranging from 8 cm to 180 cm above 60 cm away from walls) [35], and P1 - 4 are the breathing box concentration of each occupant (defined as a 500 cm^3 air volume below the nose tip) [37]. The error bars represent the standard deviation of 1-hr exposure within the ASHRAE breathing zone.

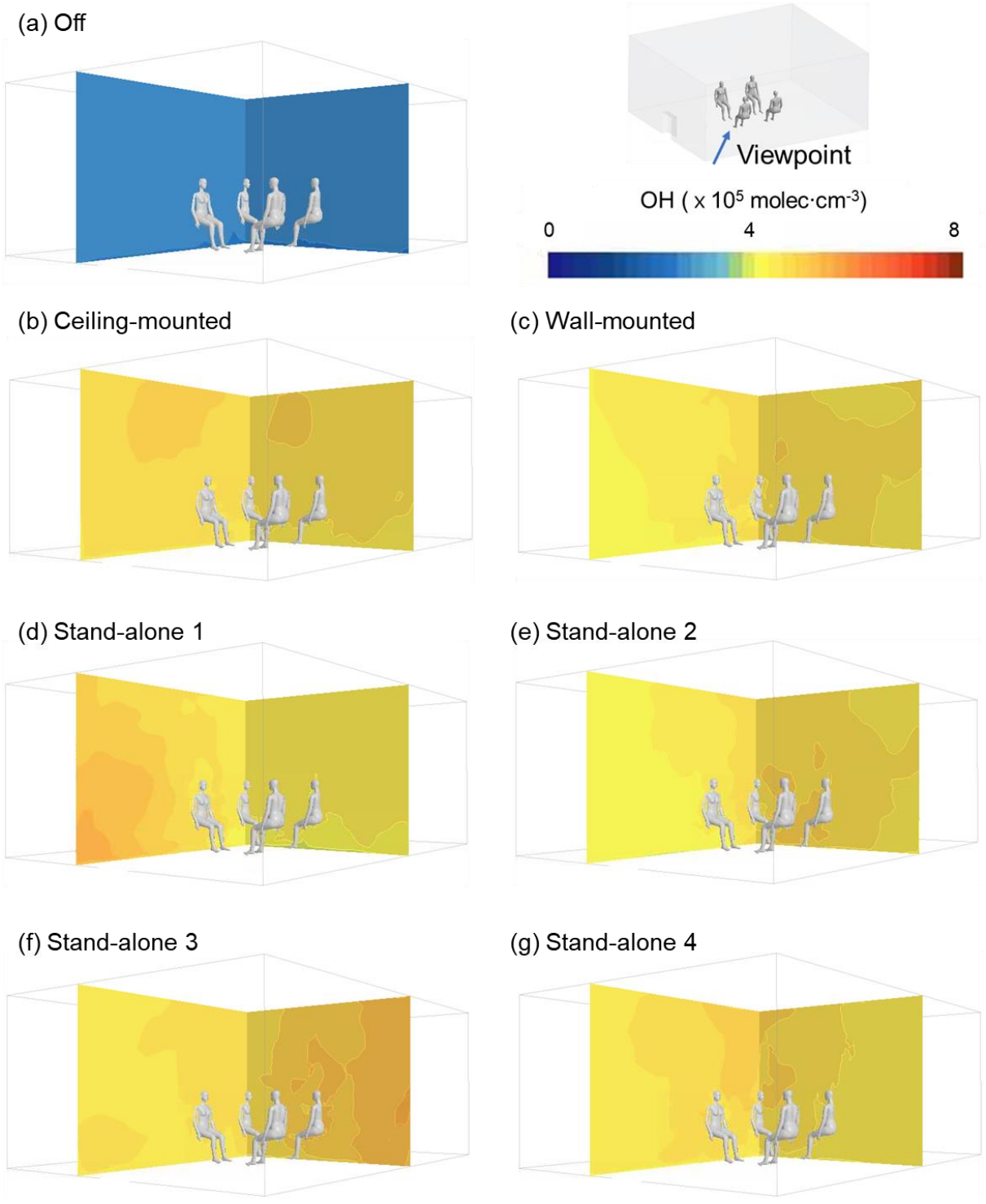

Figure S19. OH concentration contour at one hour under mixing ventilation (0.7 h^{-1}).

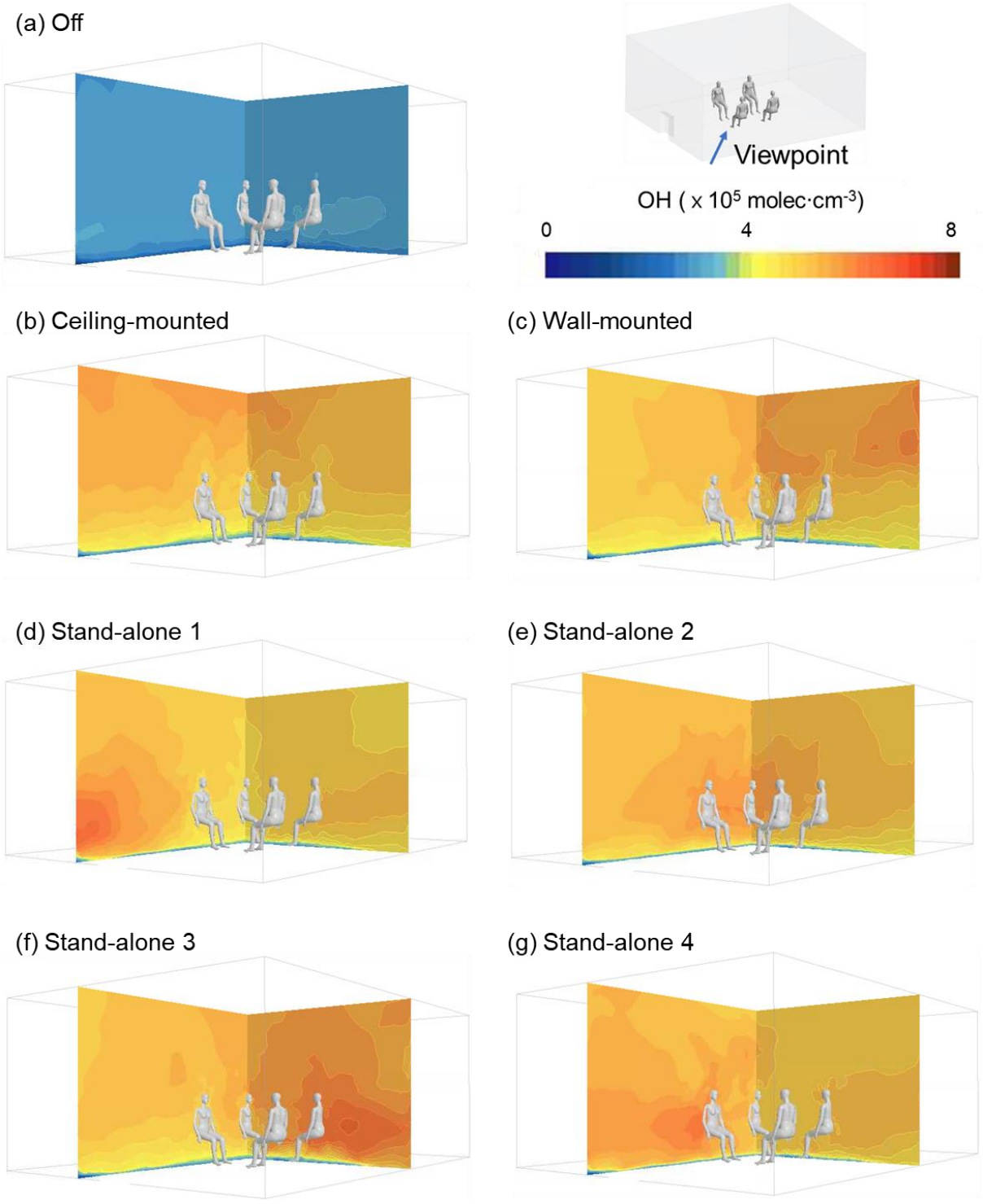

Figure S20. OH concentration contour at one hour under infiltration (0.7 h^{-1}).

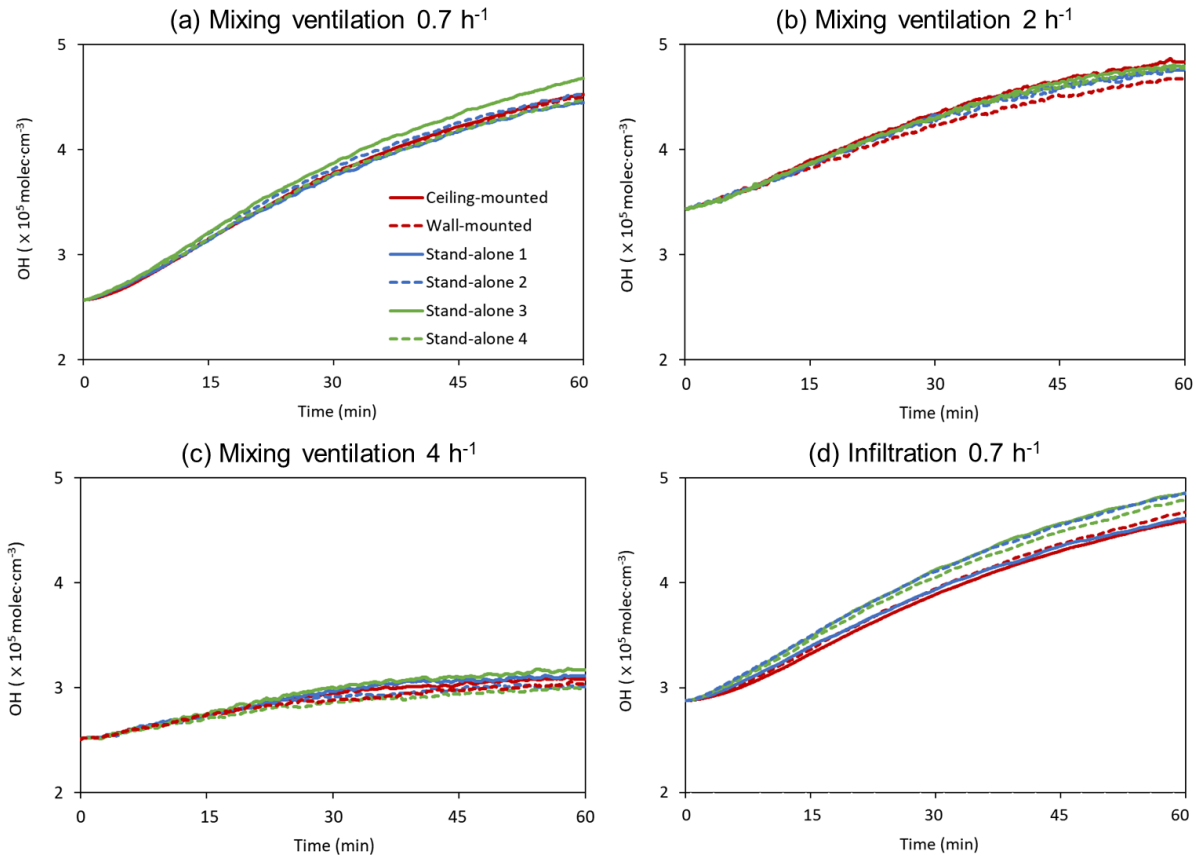

Figure S21. Time-series OH concentration within the ASHRAE breathing zone. Note that the far-UVC system activated after occupants had been in the room for one hour. Thus, the concentration at a time step of 0 represents the concentration at one hour without the far-UVC operation.

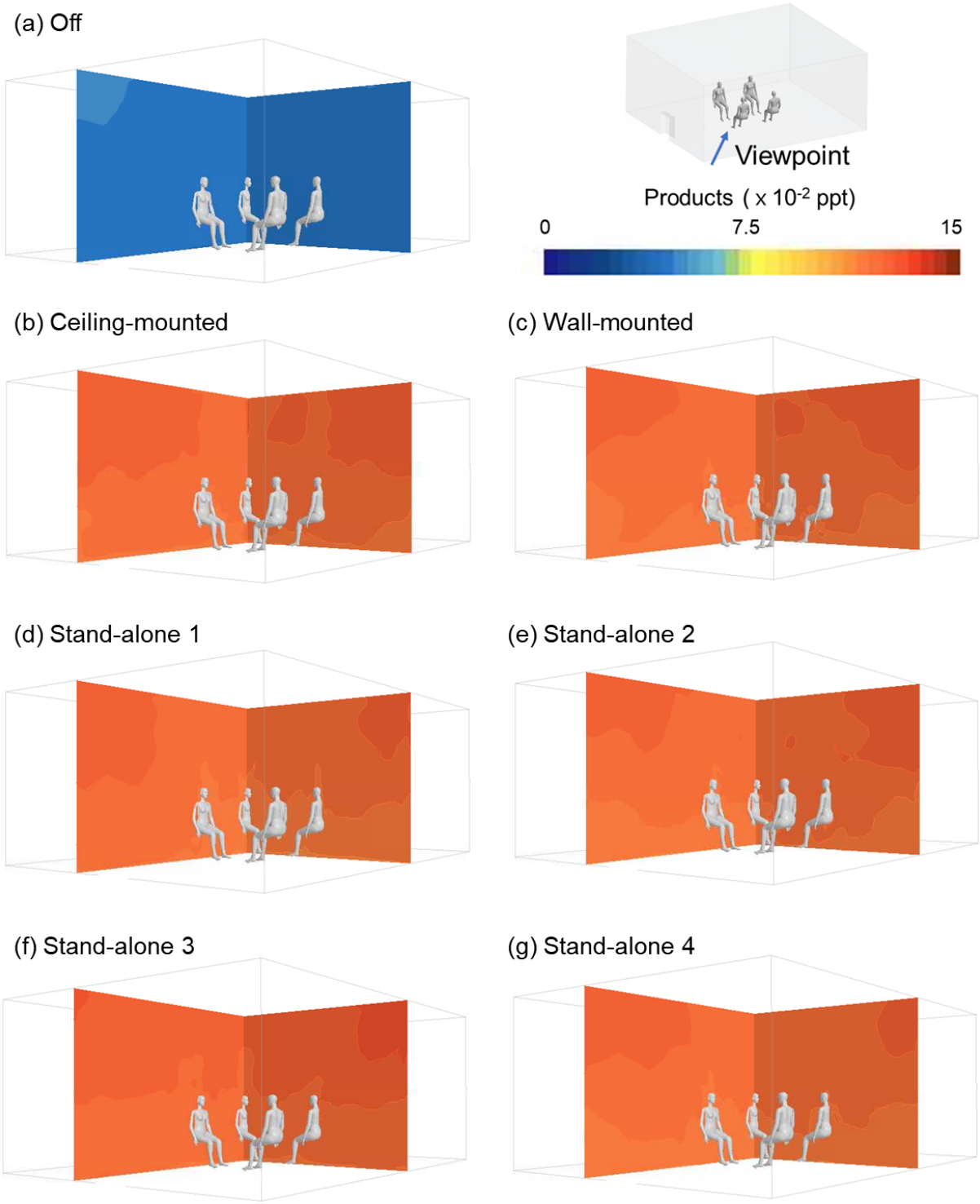

Figure S22. Products concentration contour at one hour under mixing ventilation (0.7 h^{-1}).

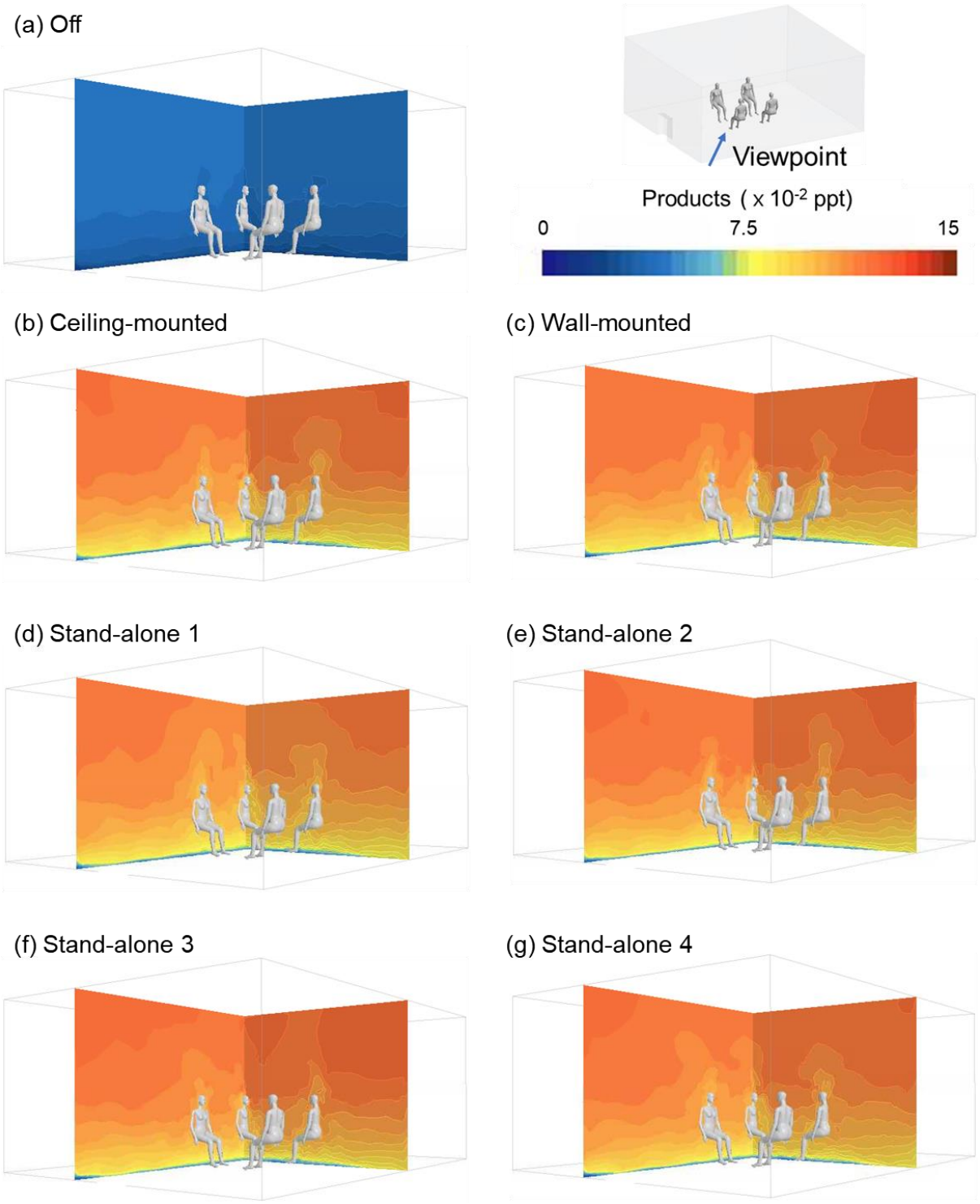

Figure S23. Products concentration contour at one hour under infiltration (0.7 h^{-1}).

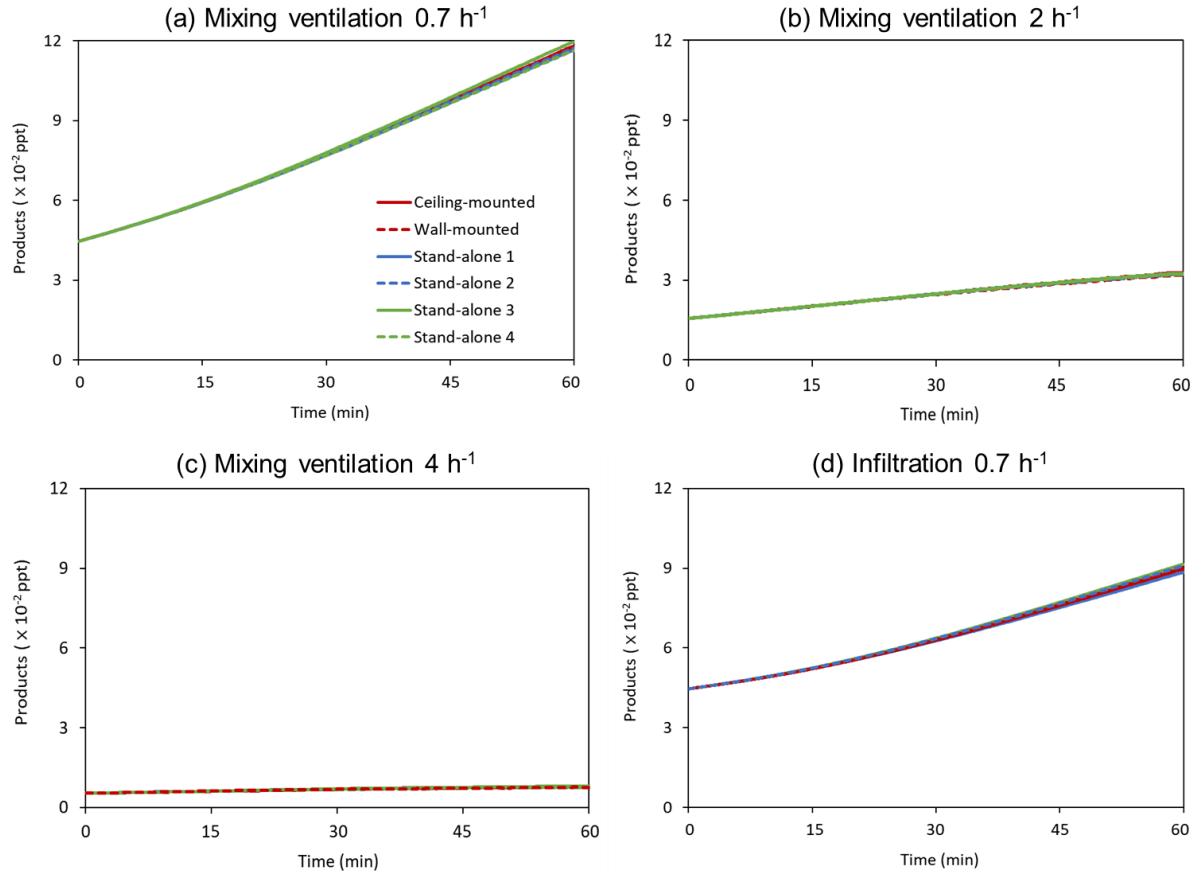

Figure S24. Time-series products concentration within the ASHRAE breathing zone. Note that the far-UVC system activated after occupants had been in the room for one hour. Thus, the concentration at a time step of 0 represents the concentration at one hour without the far-UVC operation.

References:

1. Ji, Y., Cook, M. J., Hanby, V. CFD modelling of natural displacement ventilation in an enclosure connected to an atrium. *Build. Environ*. **2007**, 42 (3), 1158-1172. https://doi.org/10.1016/j.buildenv.2005.11.002
2. Wang, Y., Zhao, F. Y., Kuckelkorn, J., Liu, D., Liu, J., Zhang, J. L. Classroom energy efficiency and air environment with displacement natural ventilation in a passive public school building. *Energy Build*. **2014**, 70, 258-270. https://doi.org/10.1016/j.enbuild.2013.11.071
3. ASHRAE. Fundamentals, chapter 18: Nonresidential cooling and heating load calculations. *ASHRAE*, Atlanta. GA, USA, 2021
4. Shan, W., Rim, D. Thermal and ventilation performance of combined passive chilled beam and displacement ventilation systems. *Energy Build*. **2018**, 158, 466-475. https://doi.org/10.1016/j.enbuild.2017.10.010
5. Zhai, Z. J., Zhang, Z., Zhang, W., Chen, Q. Y. Evaluation of various turbulence models in predicting airflow and turbulence in enclosed environments by CFD: Part 1—Summary of prevalent turbulence models. *Hvac&R Research*. **2007**, 13 (6), 853-870. https://doi.org/10.1080/10789669.2007.10391459
6. Jia, Z., Ai, Z., Yang, X., Mak, C. M., Wong, H. M. Towards an accurate CFD prediction of airflow and dispersion through face mask. *Build. Environ*. **2023**, 229, 109932. https://doi.org/10.1016/j.buildenv.2022.109932
7. Ai, Z. T., Melikov, A. K. Airborne spread of expiratory droplet nuclei between the occupants of indoor environments: A review. *Indoor Air*. **2018**, 28 (4), 500-524. https://doi.org/10.1111/ina.12465
8. Morawska, L. J. G. R., Johnson, G. R., Ristovski, Z. D., Hargreaves, M., Mengersen, K., Corbett, S., Katoshevski, D. (2009). Size distribution and sites of origin of droplets expelled from the human respiratory tract during expiratory activities. *J. Aerosol Sci*. **2009**, 40 (3), 256-269. https://doi.org/10.1016/j.jaerosci.2008.11.002
9. Lai, A. C., Nazaroff, W. W. Modeling indoor particle deposition from turbulent flow onto smooth surfaces. *J. Aerosol Sci*. **2000**, 31 (4), 463-476. https://doi.org/10.1016/S0021-8502(99)00536-4
10. Sosnowski, M., Krzywanski, J., Grabowska, K., Gnatowska, R. Polyhedral meshing in numerical analysis of conjugate heat transfer. *EPJ Web Conf*. **2018**, 180, 02096. https://doi.org/10.1051/epjconf/201818002096
11. Pei, G., Rim, D. Quality control of computational fluid dynamics (CFD) model of ozone reaction with human surface: Effects of mesh size and turbulence model. *Build. Environ*. **2021**, 189, 107513. https://doi.org/10.1016/j.buildenv.2020.107513
12. Barber, V. P., Goss, M. B., Franco Deloya, L. J., LeMar, L. N., Li, Y., Helstrom, E.; Kroll, J. H. Indoor Air Quality Implications of Germicidal 222 nm Light. *Environ. Sci. Technol*. **2023**, 57 (42), 15990-15998. https://doi.org/10.1021/acs.est.3c05680
13. Won, Y., Lakey, P. S., Morrison, G., Shiraiwa, M., Rim, D. Spatial distributions of ozonolysis products from human surfaces in ventilated rooms. *Indoor air*. **2020**, 30(6), 1229-1240. https://doi.org/10.1111/ina.12700
14. Liu, S., Koupriyanov, M., Paskaruk, D., Fediuk, G., Chen, Q. Investigation of airborne particle exposure in an office with mixing and displacement ventilation. *Sustain. Cities Soc*. **2022**, 79, 103718. https://doi.org/10.1016/j.scs.2022.103718
15. Park, S., Lee, S., Yeo, M. S., Rim, D. Performance of a heat recovery ventilation system for controlling human exposure to airborne particles in a residential building. *Build. Environ*. **2023**, 239, 110412. https://doi.org/10.1016/j.buildenv.2023.110412